ck for updates

ChemPubSoc Europe
DOI: 10.1002/batt.201800045
BATTERIES & SUPERCAPS
Articles

# Orthorhombic Nanostructured $Li_2MnSiO_4/Al_2O_3$ Supercapattery Electrode with Efficient Lithium-Ion Migratory Pathway

Miranda M. Ndipingwi,[a] Chinwe O. Ikpo,[a] Ntuthuko W. Hlongwa,[a] Zolani Myalo,[a] Natasha Ross,[a] Milua Masikini,[a] Suru V. John,[a] Priscilla G. Baker,[a] Wiets D. Roos,[b] and Emmanuel I. Iwuoha*[a]

A $Li_2MnSiO_4/Al_2O_3$ nanocomposite (LMSA) was prepared as positive electrode material for aqueous supercapatteries by hydrothermal synthesis of $Li_2MnSiO_4$ nanoparticles (LMS) followed by wet chemical coating with $Al_2O_3$. Scanning electron microscopy (SEM) mapping of the spherical LMSA nanoparticles indicated a homogenous distribution of the constituent atoms. Small-angle X-ray scattering (SAXS) measurements revealed that a prominent population of the nanoparticles show a center-to-center spacing of 7 nm. This is resulting in a large surface area accessible for the migration of Li-ions and efficient charge storage, leading to improved electrochemical performance as a supercapattery electrode. X-ray diffraction (XRD) and solid-state nuclear magnetic resonance spectroscopy (SS NMR) studies portrayed the orthorhombic ($Pmn2_1$) crystalline phase of the LMSA and LMS materials which provides a good migratory pathway for the Li-ions. The nanocomposite showed a high rate performance as a positive electrode in an aqueous supercapattery assembled with activated carbon as the negative electrode. The hybrid cell delivered a maximum specific capacitance of 141.5 F $g^{-1}$ and a maximum specific power of 4020.8 W $kg^{-1}$ with good cyclic stability and capacitance retention of 93.6% after 100 cycles. These results the promising potential of the $Li_2MnSiO_4/Al_2O_3$ nanocomposite as candidate for advanced supercapatteries.

## 1. Introduction

Climate change and the depletion of fossil fuel reserves with the associated emissions of greenhouse gases have placed a serious demand on the sustainable development of society and the environment. This requires an urgent transition towards a low-carbon energy future based on renewable energy. Optimization of electrochemical energy storage devices such as supercapacitors and rechargeable batteries have been identified as one of the key solutions to facilitate the storage, conversion, harvesting and widespread distribution of renewable energy from the infinite but intermittent energy sources such as solar and wind energy.[1–3] Supercapatteries, which combines the high power density of supercapacitors and the high energy density of rechargeable batteries have emerged as advanced hybrid energy storage devices with superior power and energy output. This hybrid device whose behaviour is analogous to that of a supercapacitor with a high energy capability uses a capacitor-like and battery-like electrode and thus takes advantage of both capacitive and faradaic charge storage mechanisms at either the material or device level.[2,4–6] The capacitive behavior can either be like electric double layer capacitors (with non-faradaic charge storage) or pseudocapacitors (with faradaic charge storage). Various hybrid systems based on the supercapacitor-battery design (anode//cathode) have been developed. Such include $Fe_3O_4$-graphene//graphene-porous carbon,[7] $Li_4Ti_5O_{12}$//$LiFePO_4$-activated carbon,[8] activated carbon//$LiMn_2O_4$.[9] Du et al.[1] reported a hybrid supercapacitor based on activated carbon//$Li_2Ni_2(MoO_4)_3$ in 2 M LiOH electrolyte, which delivered a high energy density of 36.5 W h $kg^{-1}$ and power density of 420 W $kg^{-1}$ with capacitance retention of 68% after 10000 cycles. Also, Shao's group[5] fabricated a supercapattery cell based on activated carbon//binder-free $Co_3(PO_4)\cdot 8H_2O$ and it delivered good specific capacitance of 111.2 F $g^{-1}$, specific energy of 29.29 W h $kg^{-1}$ and specific power of 468.75 W $Kg^{-1}$ in 1 M NaOH aqueous electrolyte. Even though organic electrolytes provide a larger electrochemical window which impacts the energy capability of the hybrid systems, the safety concerns arising from their toxic and flammable nature coupled with the high cost is not satisfactory for high power applications.[10] Whereas aqueous electrolytes present several advantages such as high ionic conductivity, none or negligible volatility, greater safety and lower cost due to the simpler assembly process and the inexpensive and readily available water and water-soluble salts. Hence, with a potentially high performance cathode material, the aqueous electrolytes can be chosen as competitive candidates for supercapatteries.[10,11]

[a] M. M. Ndipingwi, C. O. Ikpo, N. W. Hlongwa, Z. Myalo, Dr. N. Ross, Dr. M. Masikini, Dr. S. V. John, Prof. P. G. Baker, Prof. E. I. Iwuoha
SensorLab
Department of Chemistry
University of the Western Cape
Bellville, 7535, Cape Town, South Africa
E-mail: eiwuoha@uwc.ac.za
[b] Prof. W. D. Roos
Department of Physics
University of the Free State
Bloemfontein, South Africa


© 2018 Wiley-VCH Verlag GmbH & Co. KGaA, Weinheim

Lithium orthosilicates, $Li_2MSiO_4$ (M = Mn, Fe, Co), have drawn considerable attention as high capacity electrode materials for Li-ion batteries[12–14] and hybrid supercapacitors[15,16] owing to their numerous appealing properties such as high theoretical capacity (~330 mAhg$^{-1}$) upon the extraction of more than one lithium ion per formula unit; excellent thermal stability resulting from the strong Si–O bond and eco-friendliness. Among the orthosilicate family of electrode materials, $Li_2MnSiO_4$ is more promising because the reversible extraction of two moles of $Li^+$ ions utilising the $Mn^{2+}/Mn^{3+}$ and $Mn^{3+}/Mn^{4+}$ redox couples is more feasible leading to high energy density. However, its amorphization upon delithiation in addition to its low intrinsic electronic conductivity and low lithium diffusion coefficient limits its reversible capacity and practical electrochemical performance.[17,18] In order to overcome these downsides, several strategies have been adopted by many researchers to improve the electrochemical performance of $Li_2MnSiO_4$ cathode material, as reviewed by Gummow's[18] and Cheng's groups.[17] These include particle size reduction, coating with conductive carbon and metal oxides ($TiO_2$, ZnO), partial substitution of manganese cations with $Fe^{2+}$, $Mg^{2+}$, $Cr^{3+}$, $Al^{3+}$ and $La^{3+}$ as well as the use of nano-synthetic methods such as hydrothermal, sonochemical and solvothermal procedures. It is evident from these reports that the synthetic route as well as the homogenous reduction in particle size and the relative purity of the synthesized materials can greatly improve their reversible capacity and the overall electrochemical performance. Karthikeyan and co-workers have fabricated orthosilicate hybrid supercapacitors based on $Li_2MnSiO_4$[15] and $Li_2FeSiO_4$[16] as negative electrodes and activated carbon as the positive electrode in non-aqueous electrolytes. These hybrid cells delivered moderate specific capacitance values of 43 F g$^{-1}$ and 49 F g$^{-1}$ at a current density of 1 mA cm$^{-2}$ with specific energy and power of 43 W h kg$^{-1}$ and 200 W Kg$^{-1}$. Even though the electrochemical performance of $Li_2MnSiO_4$ cathode material has been significantly improved, further improvements are necessary to overcome some of its fundamental challenges and to meet the requirements of next generation energy storage devices. To the best of our knowledge, no extensive studies have been dedicated to the investigation of $Li_2MnSiO_4$ and nanocomposites as positive electrodes for aqueous supercapacitor-battery systems.

Herein, we report a lithium manganese silicate/alumina – $Li_2MnSiO_4/Al_2O_3$ (LMSA) nanocomposite prepared by hydrothermal synthesis with a subsequent wet chemical coating process. Various physical parameters were obtained and the LMSA electrode material was tested electrochemically in a three electrode cell and as a positive electrode for a supercapattery (two electrode cell) with activated carbon as the negative electrode in 1.0 M $LiNO_3$ aqueous electrolyte. The hybrid cell showed a specific capacitance of 117.5 F g$^{-1}$, a high specific power of 864.5 W kg$^{-1}$ at a current density of 1 A g$^{-1}$ and a capacitance retention of 93% after 100 cycles.

## 2. Results and Discussion

### 2.1. Structural and Morphological Characterization

X-ray diffraction (XRD) was used to ascertain the crystal structure and phase purity of the LMS and nanocomposite LMSA cathode materials. Figure 1 (a) below shows the XRD pattern of these materials taken at a 2θ range of 10–90°. The sharp and intense peaks indicate the crystalline nature of the materials.[19] Both samples can be indexed to the basis of the orthorhombic $Li_2MnSiO_4$ phase with the $Pmn2_1$ space group which is predicted to be iso-structural with the low temperature $Li_3PO_4$ phase.[20] These results are in good agreement with previous reports by Liu, Mancini and Swietoslawski et al.[20–21] In addition to the main Bragg peaks of the orthorhombic $Li_2MnSiO_4$ polymorph, two other unremarkable peaks at 36.3° and 43.9° can be identified in the XRD pattern of the LMS with lower intensities in the LMSA cathode materials. These peaks can be ascribed to the $MnSiO_4$ and MnO impurities, which were also observed in previous reports.[21–22] In the X-ray diffractograms of the LMS and LMSA, the latter appears to be weaker with minor and overlapping peaks at 46.2° and 51.59° corresponding to the alpha alumina ($\alpha$-$Al_2O_3$) nanoparticles phase. This is attributed to the presence of the alumina coating on the surface of the LMS nanoparticles which prevented the growth of the pristine nanoparticle grains leading to a decrease in particle size.[20] The average crystallite size was calculated from the (210) Bragg peak, using Scherrer's formula, Equation (1) below.

$$D = {}^{K\lambda}/_{\beta Cos\theta} \quad (1)$$

where $D$ is the mean crystallite size, $K$ is the shape factor constant (0.89), λ is the wavelength of the X-rays, β is the full width at half maximum (FWHM) of the (210) Bragg peak and θ is the angle of reflection of the (210) peak. The calculated grain sizes were at 16 nm for LMS and 14 nm for LMSA.

Supplementary evidence for the structures of the synthesized materials was obtained using Fourier Transform Infrared Spectroscopy (FTIR) at a resolution of 4 cm$^{-1}$. Figure 1 (b) below is the FTIR spectra of $Al_2O_3$ nanoparticles, the pristine and nanocomposite cathode materials. Bands corresponding to the internal vibration of the silicate anions according to previous work by Xie et al. resonate in the range of 400–2400 cm$^{-1}$.[23] Collected spectra are presented in the region 400–2000 cm$^{-1}$. The main absorption features at 1006 cm$^{-1}$ and around 489 cm$^{-1}$ can be assigned to the asymmetric and symmetric vibrations of the Si-O–Si bonds in the silicate tetrahedra ($SiO_4^{4-}$).[24] The distinct and sharp band at 852 cm$^{-1}$ can be assigned to the vibration of the Si–O–Mn linkage, thus confirming the complete incorporation of Mn ions into the Si–O framework. The bands at 1071 cm$^{-1}$ can be assigned to the vibration of the Al–O–Al bonds in and from $Al_2O_3$ nanoparticles, while the band at 1654 cm$^{-1}$ is apportioned to the bending vibrations of water (H–O–H) molecules adsorbed on the surface of the $Al_2O_3$ nanoparticles.[25–26]


© 2018 Wiley-VCH Verlag GmbH & Co. KGaA, Weinheim

25666223, 2018, 6, Downloaded from https://chemistry-europe.onlinelibrary.wiley.com/doi/10.1002/batt.201800045 by University of Ulsan, Wiley Online Library on [11/11/2025]. See the Terms and Conditions (https://onlinelibrary.wiley.com/terms-and-conditions) on Wiley Online Library for rules of use; OA articles are governed by the applicable Creative Commons License

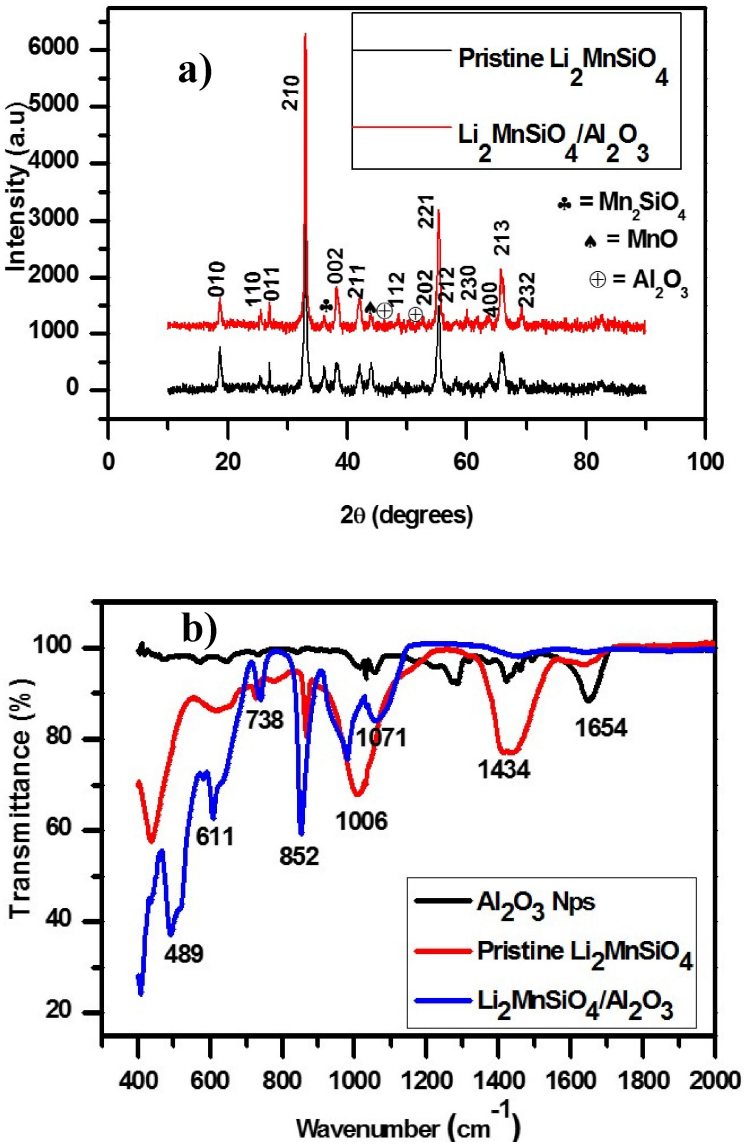


**Figure 1.** a) XRD patterns of pristine LMS and LMSA cathodes, b) FTIR spectra of $Al_2O_3$ Nps, LMS and LMSA cathode materials.

Morphological features of the LMS and LMSA cathode materials were obtained from scanning electron microscopy (SEM) as shown in Figure 2 (a) and (b) below. The nanoparticles consist of roughly uniform aggregated spherical morphologies with particle sizes in the range of 14–33 nm, average diameter of 24 nm, and a standard deviation of 5 nm for the LMS cathode material and particle size range of 15–41 nm, average diameter of 33 nm, and standard deviation of 4 nm for the LMSA cathode material. It is evident that the surface morphology of the primary particles has not been altered by coating with $Al_2O_3$ nanoparticles except for a slight increase in the degree of aggregation for the nanocomposite cathode material. The particle sizes were calculated using a Java-based image processing program known as "ImageJ". The diameter of each primary particle is defined as the length of the line which bisected the image of the particle and was fixed for all measurements, with the values analyzed numerically. The nearly spherical and aggregated morphologies of the pristine and nanocomposite cathode materials obtained from SEM were also observed in high resolution transmission electron microscopy (HRTEM) analysis. Figure 2 (c) and (e) below displays the HRTEM micrographs of LMS and LMSA cathode materials with the insets (d) and (f) representing their respective lattice fringes which reveal the crystalline nature of the materials. A nano-amorphous layer (g) ~2 nm thick is observed on the lattice fringes of the novel nanostructured cathode material, thus further confirming the presence of an alumina nano-coating in the LMSA cathode material.

A comparison of the particle size obtained from XRD and SEM/TEM analyses indicates that the average crystallite size calculated from the XRD peak FWHM is smaller than that obtained from SEM/TEM. This is because microscopic imaging techniques provide information on the average physical sizes of primary and secondary particles (in the case of agglomeration), while XRD gives the calculated sizes of the crystalline domains. Since a single grain can contain several domains with different


© 2018 Wiley-VCH Verlag GmbH & Co. KGaA, Weinheim

25666223, 2018, 6, Downloaded from https://chemistry-europe.onlinelibrary.wiley.com/doi/10.1002/batt.201800045 by University of Ulsan, Wiley Online Library on [11/11/2025]. See the Terms and Conditions (https://onlinelibrary.wiley.com/terms-and-conditions) on Wiley Online Library for rules of use; OA articles are governed by the applicable Creative Commons License

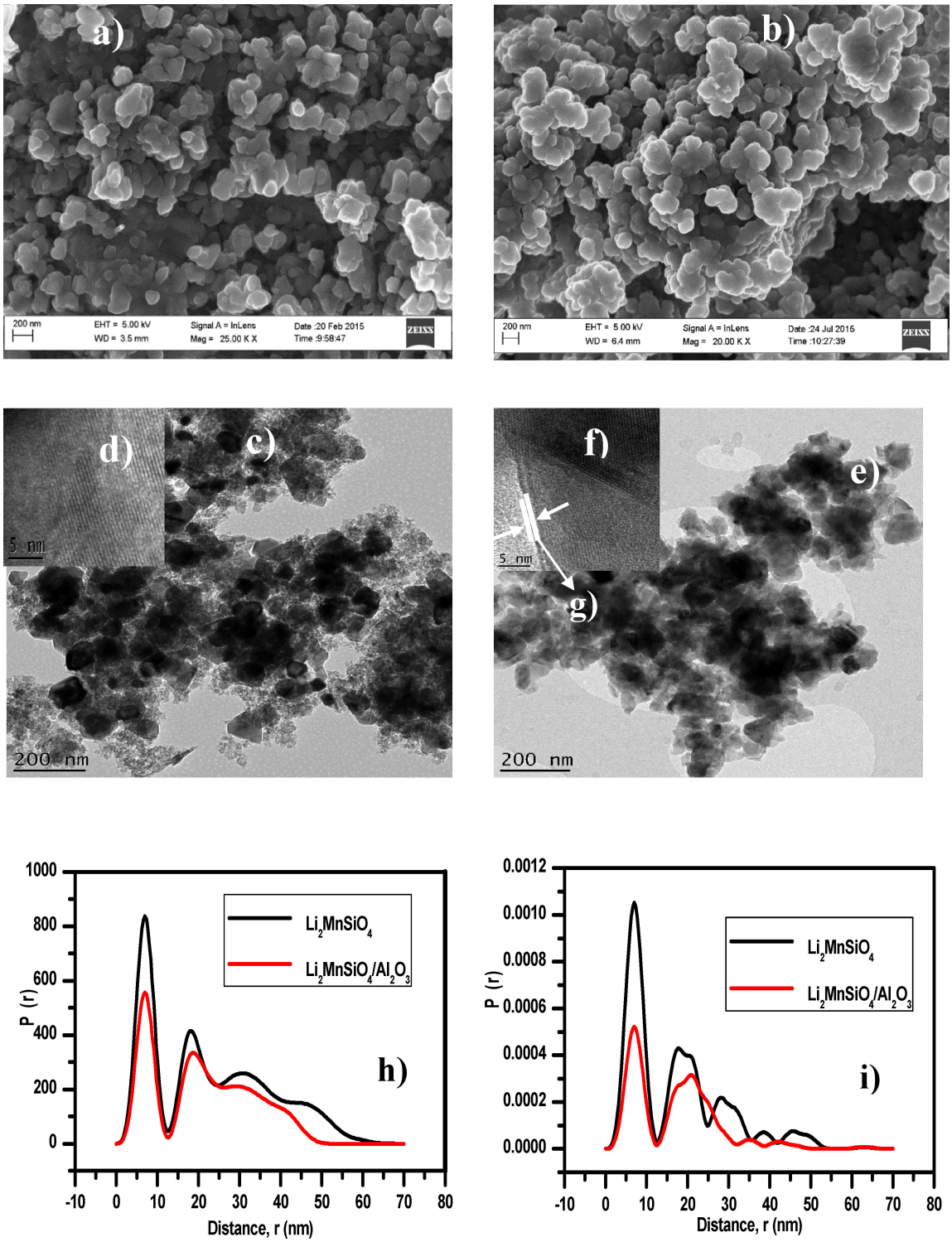


**Figure 2.** SEM micrographs of a) LMS, b) LMSA; HRTEM images of c) LMS, e) LMSA; and SAXS particle size distribution in h) number weighted and i) volume weighted.

orientations, it is expected that particle size obtained from SEM/TEM will be greater than that obtained from XRD measurement.

Small-angle X-ray scattering (SAXS) was used to further investigate the particle size distribution of the pristine and nanocomposite cathode materials. The pair distance distribution functions (PDDF) of these materials in volume-weighted and number-weighted particle size distributions are shown in Figure 2 (h) and (i) below, respectively. It can be observed that the scattering cross-sections describe nanoparticles with an upper limit in real space at 60 ± 5 nm for LMS and 70 ± 3 nm for LMSA. Although the maximum particle sizes from SAXS are at


© 2018 Wiley-VCH Verlag GmbH & Co. KGaA, Weinheim

25666223, 2018, 6, Downloaded from https://chemistry-europe.onlinelibrary.wiley.com/doi/10.1002/batt.201800045 by University of Ulsan, Wiley Online Library on [11/11/2025]. See the Terms and Conditions (https://onlinelibrary.wiley.com/terms-and-conditions) on Wiley Online Library for rules of use; OA articles are governed by the applicable Creative Commons License

60 ± 5 nm for LMS and 70 ± 3 nm for LMSA, a breakdown of the volume weighted, and the number weighted particle size distributions show that a prominent population of the nanoparticles have a center-to-center spacing of 7 nm, followed by 21 and 30 nm. This trend follows that obtained from the SEM images, but the slight change in particle sizes is because SAXS provides more accurate and detailed information as opposed to SEM which offers a relatively small sample portion of interest.[27–28] The larger particles are interpreted as aggregates of the smaller nanoparticles as observed in the SEM images.

Energy dispersive spectroscopy (EDS) and the elemental mappings of the nanocomposite cathode material are presented in Figure 3 below. Figure 3 (a) shows the SEM image of LMSA obtained at a lower magnification (1 μm). As can be seen from the EDS spectra; Figure 3 (b), all the constituent elements are present. The presence of palladium and gold emanated from a conductive palladium-gold alloy which was coated on the surface of the samples to increase contrast during analysis, while carbon came from the carbon black adhesive used on the sample holders. Elemental mappings; Figure 3 (c-f), of the nanocomposite cathode material showed an even distribution of the elements (O, Si, Mn and Al) over the enitire sample. This uniform distribution of elements provided fast removal and

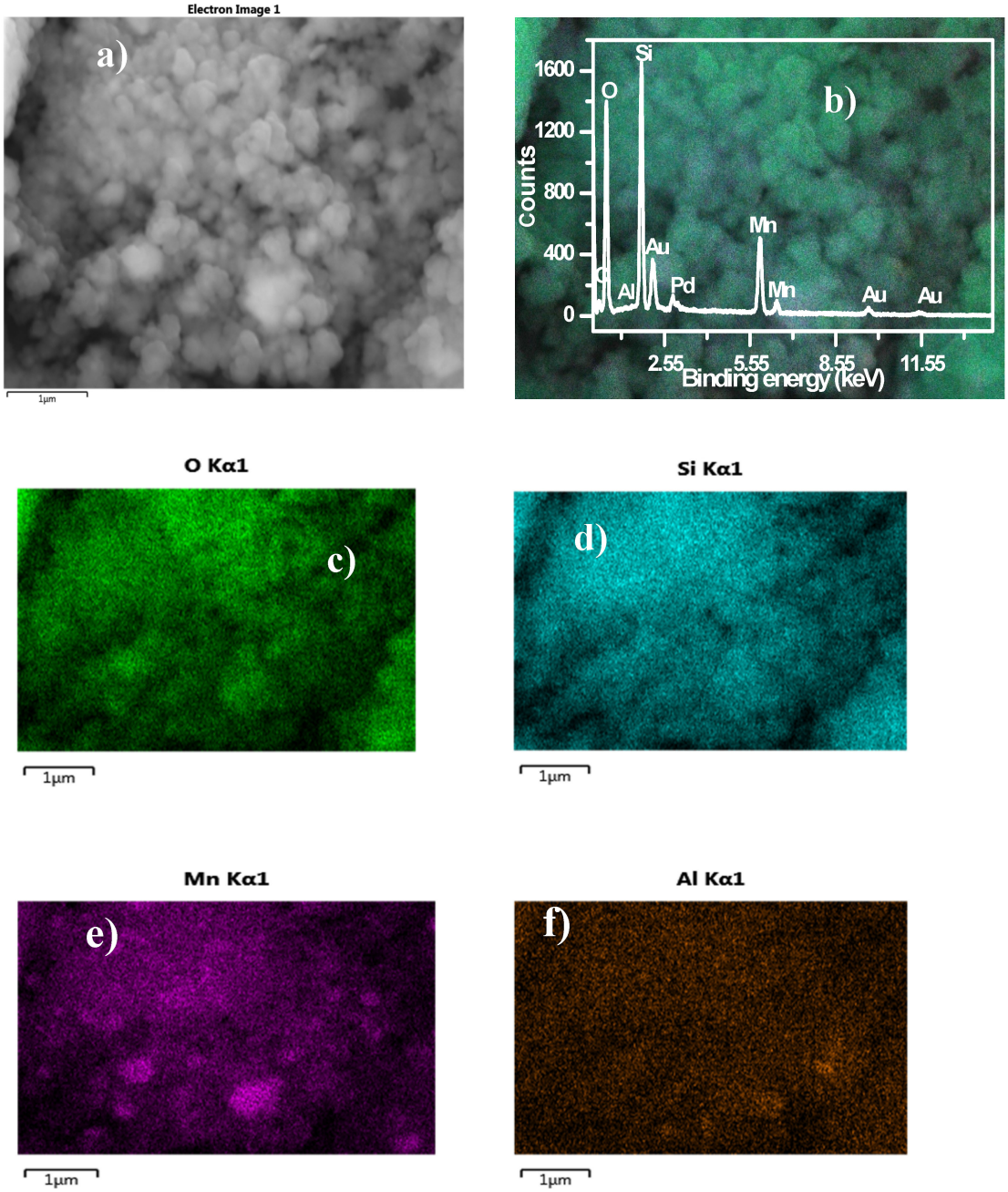


**Figure 3.** SEM image of LMSA obtained at lower magnification (a); EDS and electron layered image of LMSA (b); Elemental distribution mapping of O (c), Si (d), Mn (e) and Al (f).


© 2018 Wiley-VCH Verlag GmbH & Co. KGaA, Weinheim

25666223, 2018, 6, Downloaded from https://chemistry-europe.onlinelibrary.wiley.com/doi/10.1002/batt.201800045 by University of Ulsan, Wiley Online Library on [11/11/2025]. See the Terms and Conditions (https://onlinelibrary.wiley.com/terms-and-conditions) on Wiley Online Library for rules of use; OA articles are governed by the applicable Creative Commons License

insertion of $Li^+$ ions from and into the nanostructured LMSA crystalline structure.[12]

### 2.2. Surface Chemistry and Lithium Local Environment

X-ray photoelectron spectroscopy (XPS) was used to confirm further details on the composition and oxidation states of the metal cations present in the LMS and LMSA cathode materials. Figure 4 above shows the XPS spectra of LMS and LMSA. The binding energy of $Mn2p_{3/2}$ at 643.5 eV (a) for LMS and at 643.0 eV (b) for LMSA is consistent with that of $Mn^{2+}$, confirming that the divalent state of manganese is present in our samples.[29–31] The binding energy of Si2p at 102.6 eV (c) and 102.7 eV (d) for LMS and LMSA cathode materials, respectively is also in line with that of $Si^{4+}$ in polysiloxanes, indicating the formation of the orthosilicate [$SiO_4$] structure.[24–32] The XPS spectra of LMSA also shows that the binding energy of Li1s at 55.5 eV (e) and that of Al2p at 74.7 eV is in agreement with that of $Li_2CO_3$ and $Al_2O_3$, respectively.[32–33]

The lithium local environment with structural and electronic anisotropies of the as-prepared materials was explored using Solid-state Nuclear Magnetic Resonance (SS NMR) Spectroscopy. Figure 5 below shows the SS NMR spectra of LMS and LMSA cathode materials. Both spectra are dominated by the interaction of the lithium nuclei with magnetic moments of the unpaired electron spins.[34] The unpaired electrons of the tetrahedrally-coordinated high-spin $Mn^{2+}$ ions in $Li_2Mn^{2+}SiO_4$ with a $d^5$ electronic configuration are present in the $eg^2t_2g^3$ configuration, giving rise to an isotropic contribution known as the Fermi-contact shift which results in the isotropic peaks.[34–36] In addition, the spin-dipolar interaction between the lithium nuclei and the unpaired electrons of the transition metal ions generate a strong dipolar coupling which leads to the broad spinning sidebands. The $^7$Li-NMR spectrum of the LMS (a) is characterized by three isotropic peaks at ~310.7, 0.8 and −306.2 ppm. The isotropic peaks at ~310.7 and −306.2 ppm arise from the majority $Pmn2_1$ polymorph,[35–38] which was observed in XRD investigations. The peak at ~0.8 ppm ascends from the ionic character of the lithium nuclei. These values are slightly shifted in the spectrum of LMSA (~310.7 and −307.5 ppm, ~0.0 ppm) due to the presence of the alumina surface coating which likely induces covalently bonded Al-O–Si species which enhanced both local and long-order fluctuations leading to slight deshielding around the lithium nuclei and a shift to higher frequencies.

### 2.3. Electrochemical Performance

The electrochemical performance of LMS and LMSA electrodes were evaluated using a three-electrode cell configuration in aqueous 1.0 M $LiNO_3$ aqueous electrolyte at a potential window of −1 to 1 V. The cyclic voltammetric (CV) profiles of LMS and LMSA are presented in Figure 6 (a). A set of redox peaks were observed for the materials indicating their non-capacitive faradaic energy storage characteristics. These peaks correspond to the charge-discharge reactions of the $Mn^{2+}/Mn^{3+}$ redox couple.

The anodic (charge) and cathodic (discharge) peak intensities of LMSA are much higher than those of LMS with charge peak current and potential values at 0.477 μA and 0.430 V, and discharge peak current and potential values at 0.117 μA and 0.117 V for LMS. The anodic peak current and potential points for LMSA were at 0.914 μA and 0.408 V and cathodic peak current and potential values were at −0.956 μA and 0.123 V, respectively. Reduced peak-to-peak potential separation (0.313 V for LMS and 0.285 V for LMSA) obtained for the nanocomposite material depicts better electrochemical reversibility of the material over the pristine. Further electrochemical investigations from the CV curves at different scan rates; Figure 6 (b) above revealed that electrode polarization increases considerably as the scan rate increases and the redox pairs become less pronounced and overlap with each other. Thus, ascertaining the quasi-reversible electron transfer process occurring on the LMS and LMSA electrodes. Charge and discharge capacity values calculated according to Equations (1) and (2) below, from the CV profiles gave charge capacities of 107. 2 mA h g$^{-1}$ (358.1 F g$^{-1}$) and 209. 1 mA h g$^{-1}$ (751.7 F g$^{-1}$) with corresponding discharge capacities of 68 mA h g$^{-1}$ (245.1 F g$^{-1}$) and 159 mA h g$^{-1}$ (358.1 F g$^{-1}$) for LMS and LMSA, respectively. These results are in good agreement with those obtained from studies in organic electrolytes.[35,36] The magnitude of the current in the linear potential sweep voltammetry is related to the number of electrons exchanged in the redox reaction, $n$; the area of the electrode, $A$ (cm$^2$); the diffusion coefficient of $Li^+$, $D_{Li}$ (cm$^2$ s$^{-1}$); concentration, $C$ (mol cm$^{-3}$) and the speed at which the potential is scanned, $\nu$ (V s$^{-1}$); by the Randles-Sevcik Equation (Equation 3).[38–41] The area (AV) is obtained by integrating the oxidative current-potential curve for the charge capacity and the reductive current-potential curve for the discharge capacity for both materials.

$$SpecificCapacity(mAhg^{-1}) = {}^{(Q)}/_{m} \times 1000 \quad (2)$$

$$Q(Ah) = {}^{Area(AV)}/_{ScanRate(Vs^{-1})} X \frac{1h}{3600s} \quad (3)$$

$$I_{pa} = 2.69 \times 10^5\, n^{3/2}\, A\, D_{Li}^{1/2}\, C\, \nu^{1/2} \quad (4)$$

where, $Q$ is the charge (C) and $m$ is the active mass of the electrode (g). The diffusion coefficient calculated according to Equation (4) from the slope of the line in the Randles-Sevcik plot; Figure 6 (c), was at $3.06\times10^{-6}$ cm$^2$ s$^{-1}$ for LMSA. This value is one order of magnitude higher than that obtained at $6.79\times10^{-7}$ cm$^2$ s$^{-1}$ for LMS. These results indicate that the presence of the $Al_2O_3$ surface coating efficiently enhanced the charge transfer kinetics leading to improved electrochemical performance of LMSA due to shorter interatomic distances in the $LiO_4$ and $SiO_4$ tetrahedra as observed from the SEM and HRTEM investigations

Electrochemical Impedance Spectroscopic (EIS) measurements were conducted on the samples to investigate the electrical resistance and diffusive processes occurring at the


© 2018 Wiley-VCH Verlag GmbH & Co. KGaA, Weinheim

25666223, 2018, 6, Downloaded from https://chemistry-europe.onlinelibrary.wiley.com/doi/10.1002/batt.201800045 by University of Ulsan, Wiley Online Library on [11/11/2025]. See the Terms and Conditions (https://onlinelibrary.wiley.com/terms-and-conditions) on Wiley Online Library for rules of use; OA articles are governed by the applicable Creative Commons License

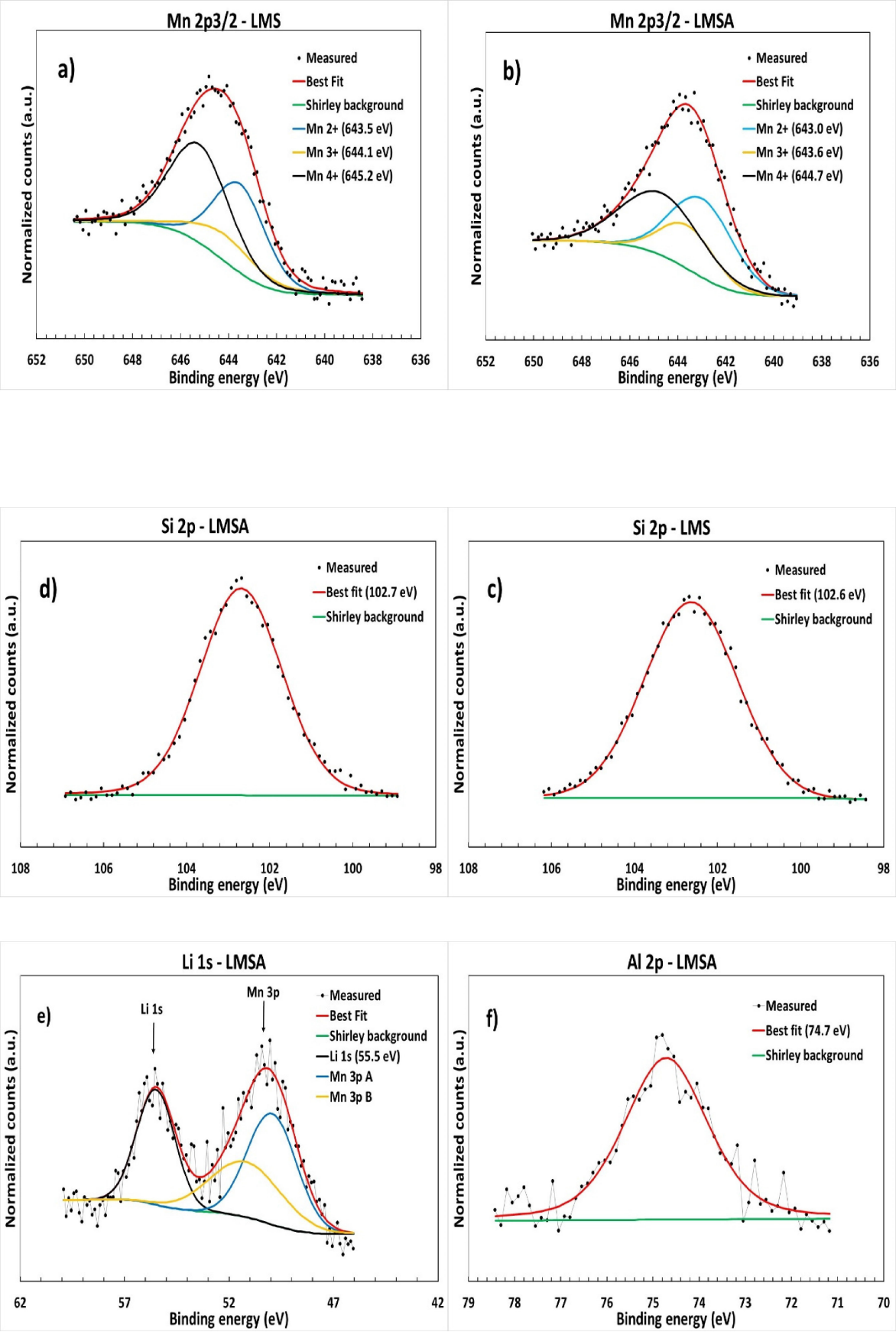


**Figure 4.** XPS spectra of: LMS (a, c) and LMSA (b, d, e, f).


© 2018 Wiley-VCH Verlag GmbH & Co. KGaA, Weinheim

25666223, 2018, 6, Downloaded from https://chemistry-europe.onlinelibrary.wiley.com/doi/10.1002/batt.201800045 by University of Ulsan, Wiley Online Library on [11/11/2025]. See the Terms and Conditions (https://onlinelibrary.wiley.com/terms-and-conditions) on Wiley Online Library for rules of use; OA articles are governed by the applicable Creative Commons License

25666223, 2018, 6, Downloaded from https://chemistry-europe.onlinelibrary.wiley.com/doi/10.1002/batt.201800045 by University of Ulsan, Wiley Online Library on [11/11/2025]. See the Terms and Conditions (https://onlinelibrary.wiley.com/terms-and-conditions) on Wiley Online Library for rules of use; OA articles are governed by the applicable Creative Commons License

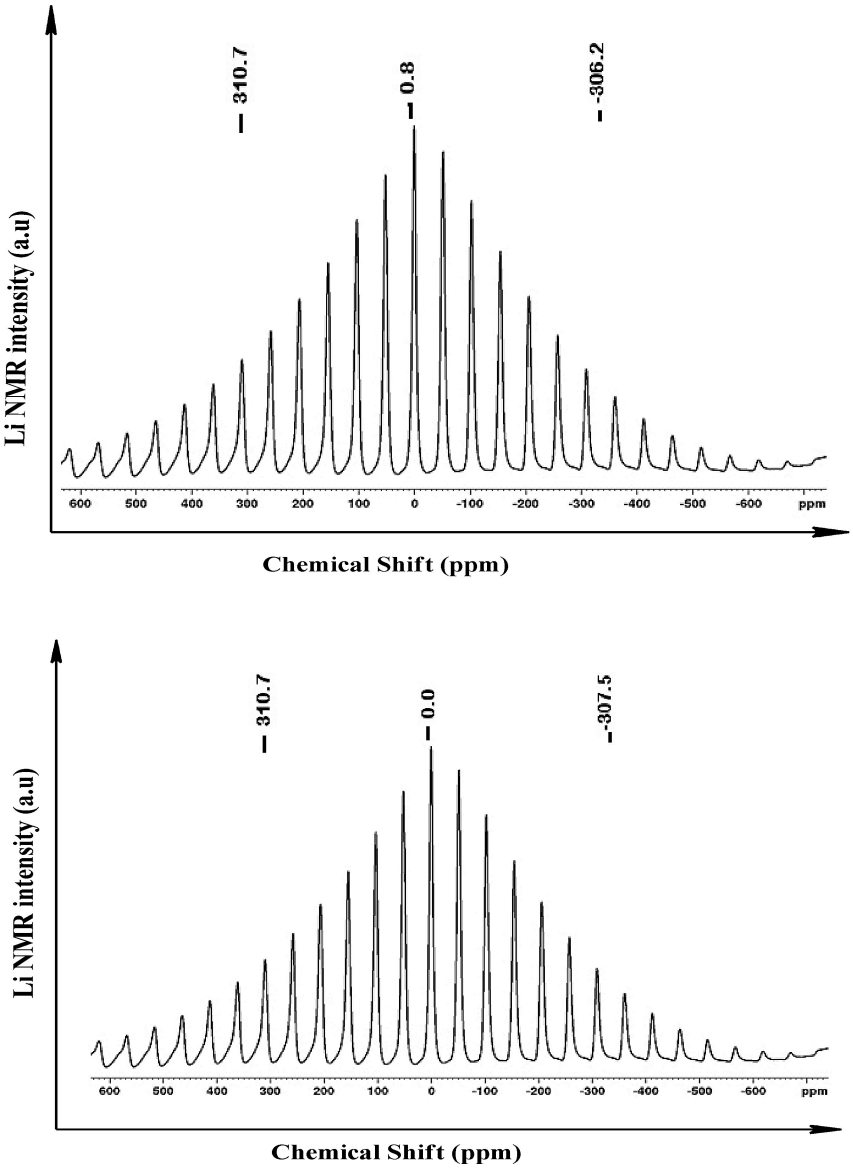


**Figure 5.** $^{7}$Li MAS NMR spectra of a) LMS and b) LMSA cathode materials at a MAS spinning speed of 10 kHz.

electrochemical interfaces of the electrodes. Figure 6 (d) shows the Nyquist plots of LMS and LMSA and the equivalent circuit model (the inset) used for fitting the EIS data. All the plots consist of a small semicircle (though not so prominent) in the high frequency region which describes the electron transfer limiting processes and an inclined line in the medium to low frequency region which provides information about the diffusion-controlled processes. The intercept at the high frequency zone along the $Z_{re}$ axis corresponds to the Ohmic/solution resistance ($R_s$), while the diameter of the semicircle along the $Z_{re}$ axis relates to the charge transfer resistance ($R_{ct}$), which was obtained after fitting the data using the equivalent circuit.

The inclined line is attributed to the diffusion of lithium ions in the bulk of the active orthosilicate material,[42] known as the Warburg diffusion ($Z_w$). All parameters obtained from the EIS modelling are recorded in Table 1 below. A higher ohmic resistance (35 66 Ω), is observed for the LMS pristine material whereas in the case of LMSA, the alumina surface coating improved the connectivity of LMS nanoparticles thereby bringing them into close proximity with good conductivity channels for electron mobility between adjacent LMS particles leading to lower ohmic resistance (25.79 Ω).[22,43] The constant phase element (*CPE*) which describes the double layer capacitance of the electrode-solution interface is a function of the electrode potential.[43] Only a slight deviation was observed for the *CPE* values of LMS and LMSA, due to a plausible activation process

**Table 1.** EIS simulation data of the LMS and LMSA cathode materials.

| Electrode | $R_s$ [Ω] | *CPE* [μF] | $R_{ct}$ [Ω] | $W_s$ [Ω/s$^{-1/2}$] |
|---|---|---|---|---|
| LMS | 35.66 | 0.926 | 1549 | 0.639 |
| LMSA | 25.79 | 0.935 | 1389 | 0.620 |


© 2018 Wiley-VCH Verlag GmbH & Co. KGaA, Weinheim

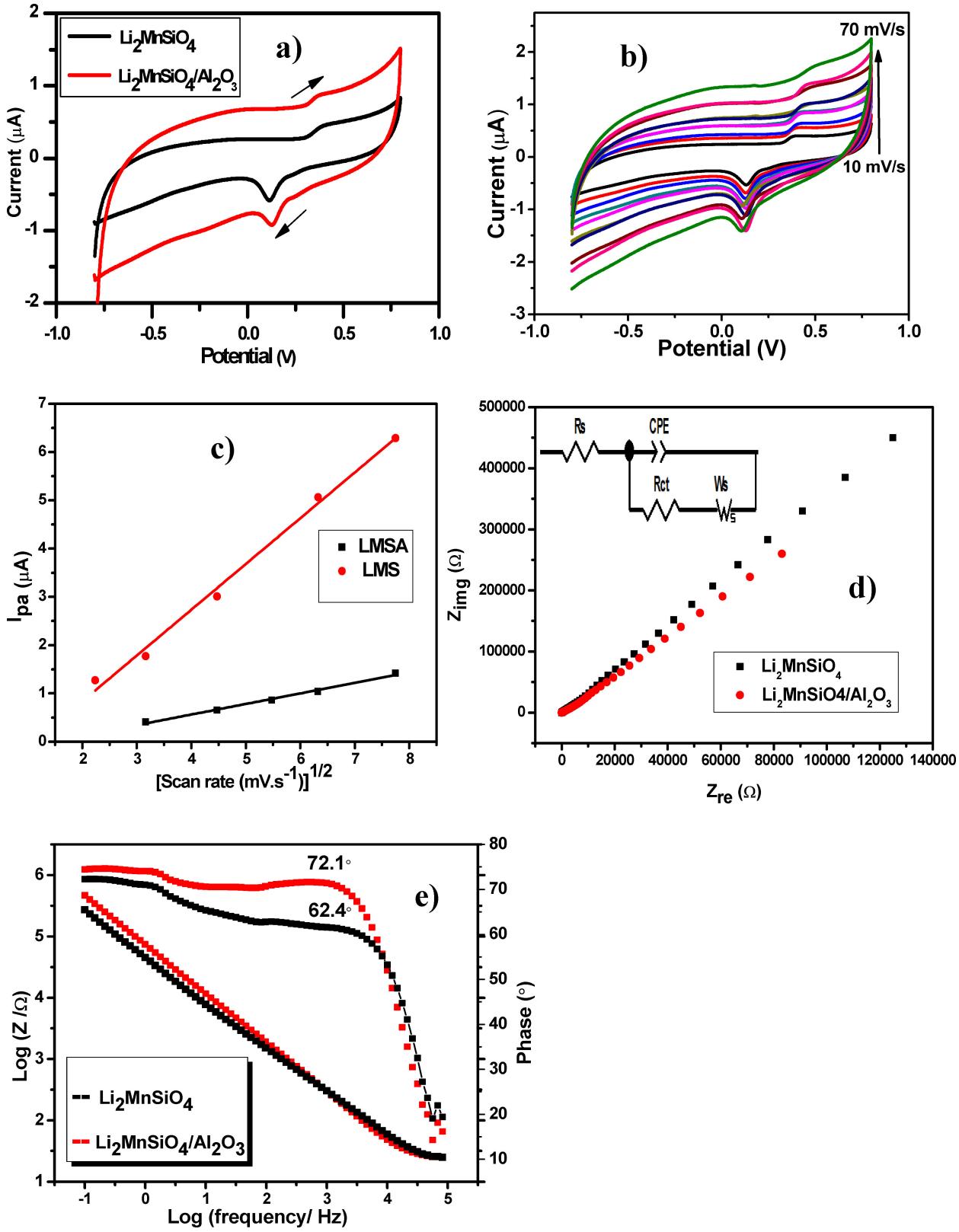


**Figure 6.** a) The cyclic voltammograms (CVs) of LMS and LMSA half cells at 10 mV/s. b) The scan rate dependency in CVs of LMSA electrodes. c) Randles-Sevcik plots of the normalized anodic peak current for LMSA and LMS half cells, d) The Nyquist plots of LMS and LMSA and the equivalent circuit (inset) used for the EIS data fitting; and e) the Bode plots of LMS and LMSA half cells.


© 2018 Wiley-VCH Verlag GmbH & Co. KGaA, Weinheim

25666223, 2018, 6, Downloaded from https://chemistry-europe.onlinelibrary.wiley.com/doi/10.1002/batt.201800045 by University of Ulsan, Wiley Online Library on [11/11/2025]. See the Terms and Conditions (https://onlinelibrary.wiley.com/terms-and-conditions) on Wiley Online Library for rules of use; OA articles are governed by the applicable Creative Commons License

induced by the $Al_2O_3$ passivating layer on the surface of LMS.[44] Furthermore, the charge transfer resistance of the LMSA (1389 Ω) was found to be lower than that of the LMS (1549 Ω), indicating that the electronic conductivity of the LMS was considerably improved as a result of the alumina surface coating. Figure 6 (e) is a presentation of the Bode plots of LMS and LMSA. LMSA presented a path of least impedance to the flow of current with a phase angle of 72.1° at higher frequencies, while LMS showed a relatively high resistance to the flow of current with a phase angle of 62.4° at higher frequencies. These phase angle values further confirm the higher conductivity of LMSA over LMS, as seen from the $R_{ct}$ values. The Warburg diffusion ($W_s$) observed in the LMSA electrode can be described as a transmitting boundary, whereby the diffusion specie ($Li^+$) is easily consumed at the electrode. And the Warburg diffusion in LMS can be described as an almost reflecting boundary, whereby the discharge of $Li^+$ is slow in the LMS electrode.

To investigate the feasibility of the LMSA nanocomposite for practical energy storage applications, we assembled a hybrid supercapattery based on nanocomposite LMSA as the positive electrode and activated carbon as the negative electrode separated by a polypropylene film in 1.0 M $LiNO_3$ electrolyte. The hybrid cells were also constructed using the pristine positive electrode material for comparative studies. Figure 7 (a) below shows the CV plots of the aqueous hybrid AC//$Li_2MnSiO_4/Al_2O_3$ cells at different scan rates from 5 to 70 $mVs^{-1}$. The almost irregular shapes of the CV curves displayed the dominant capacitive behavior of the supercapattery.[2] Furthermore, the CV curves retain their original shape with increasing scan rate, revealing the good rate capability and desirable performance of the supercapattery.

Figure 7 (b) above reveals the galvanostatic charge-discharge profiles of the AC//$Li_2MnSiO_4/Al_2O_3$ aqueous supercapattery at various current loads at a potential window of 1.6 V. As observed in the CV curves, the dominant capacitor-like behaviour of the aqueous supercapattery is demonstrated. The charge-discharge profiles deviate slightly from the potential plateaus observed with majority battery behaviour, with quasi-lined curves confirming that our hybrid system exhibits the charge-discharge performance of a combination of a battery and a supercapacitor.[5,45] The AC//$Li_2MnSiO_4/Al_2O_3$ aqueous supercapattery shows more than twice the discharging time as illustrated on Figure 7 (c), for an aqueous hybrid cell assembled using the pristine material (AC//$Li_2MnSiO_4$). The specific capacitance $C_{sp}$ ($F\,g^{-1}$), specific energy $E$ ($W\,h\,Kg^{-1}$) and specific power $P$ ($W\,kg^{-1}$) were obtained from the discharge curves using Equations (5)–(7) below.[7]

$$C_{sp} = \frac{4I}{m\Delta V/\Delta t} \tag{5}$$

$$E = \frac{1}{2} C_{sp} V^2 \tag{6}$$

$$P = E/\Delta t \tag{7}$$

where $I$ is the applied current (A), $m$ is the total mass of both electrodes (g), $\Delta V/\Delta t$ is the slope obtained by fitting a straight line to the discharge curve ($V\,s^{-1}$) and $V$ is the maximum potential.

The hybrid cells showed a specific capacitance of 117.5 $F\,g^{-1}$ at a current load of 1 $A\,g^{-1}$. The cyclic stability of the supercapattery cells was investigated by repeated charge-discharge cycles. The number of cycles was limited by equipment. The supercapattery maintained a specific capacitance of 109.7 $F\,g^{-1}$ after 100 cycles as shown on Figure 7 (d), with capacitance retention of 93.36%. Thus, indicating the good cyclic stability of the hybrid cell. To further evaluate the charge storage mechanism of the AC//$Li_2MnSiO_4/Al_2O_3$ aqueous supercapattery, specific capacity values were determined at different current loads as shown on Figure 7 (f). Interestingly, the more desirable rate capability obtained from the supercapattery was that of the capacitive charge storage, which is in line with our cyclic voltammetric studies.

The Ragone plot of the AC//$Li_2MnSiO_4/Al_2O_3$ aqueous supercapattery is shown on Figure 7 (g). A specific energy of 12.5 $W\,h\,kg^{-1}$ was obtained at a specific power of 407.2 $W\,kg^{-1}$ and current load of 0.5 $A\,g^{-1}$. Even at a current load of 5 $A\,g^{-1}$ with a high specific power of 4020.8 $W\,kg^{-1}$, a specific energy of 4 $W\,h\,kg^{-1}$ was delivered by the AC//$Li_2MnSiO_4/Al_2O_3$ supercapattery. Compared to the electrochemical performance of other reported hybrid devices, the AC//$Li_2MnSiO_4/Al_2O_3$ aqueous supercapattery delivered an increased specific capacitance and specific power almost three times greater than some reported values[15,16] and these results agree with those obtained from AC//binder-free $Co_3(PO_4)\cdot 8H_2O$[6] and NiO-$In_2O_3$//NiO-$In_2O_3$[5] systems. Overall, the AC//$Li_2MnSiO_4/Al_2O_3$ aqueous supercapattery showed excellent specific capacitance, suitable specific energy, high specific power and good capacitance retention and cycling stability.

## 3. Conclusions

The synthesis and characterization of nano-alumina surface coated $Li_2MnSiO_4$ is reported for the first time. The nanocomposite cathode material was prepared through a hydrothermal synthetic protocol. The XRD and SS NMR showed that the LMSA cathode material can be indexed to the orthorhombic crystal pattern with the $Pmn2_1$ space group. Morphological and SAXS studies revealed spherically shaped nanoparticles with average diameters of 24 nm and a prominent population of the nanoparticles having a center-to-center spacing of 7 nm. This provided a large surface area for the migration of Li-ions and efficient charge storage, leading to better electrochemical performance as a supercapattery electrode. The nanocomposite $Li_2MnSiO_4/Al_2O_3$ illustrated faradaic charge storage in a three-electrode system with 1.0 M $LiNO_3$ aqueous electrolyte and a dominant capacitive behavior in a supercapattery cell assembled using our nanocomposite as the positive electrode and activated carbon as the negative electrode. The AC//$Li_2MnSiO_4/Al_2O_3$ aqueous supercapattery delivered a high specific capacitance of 117.5 $F\,g^{-1}$, specific energy of


© 2018 Wiley-VCH Verlag GmbH & Co. KGaA, Weinheim

25666223, 2018, 6, Downloaded from https://chemistry-europe.onlinelibrary.wiley.com/doi/10.1002/batt.201800045 by University of Ulsan, Wiley Online Library on [11/11/2025]. See the Terms and Conditions (https://onlinelibrary.wiley.com/terms-and-conditions) on Wiley Online Library for rules of use; OA articles are governed by the applicable Creative Commons License

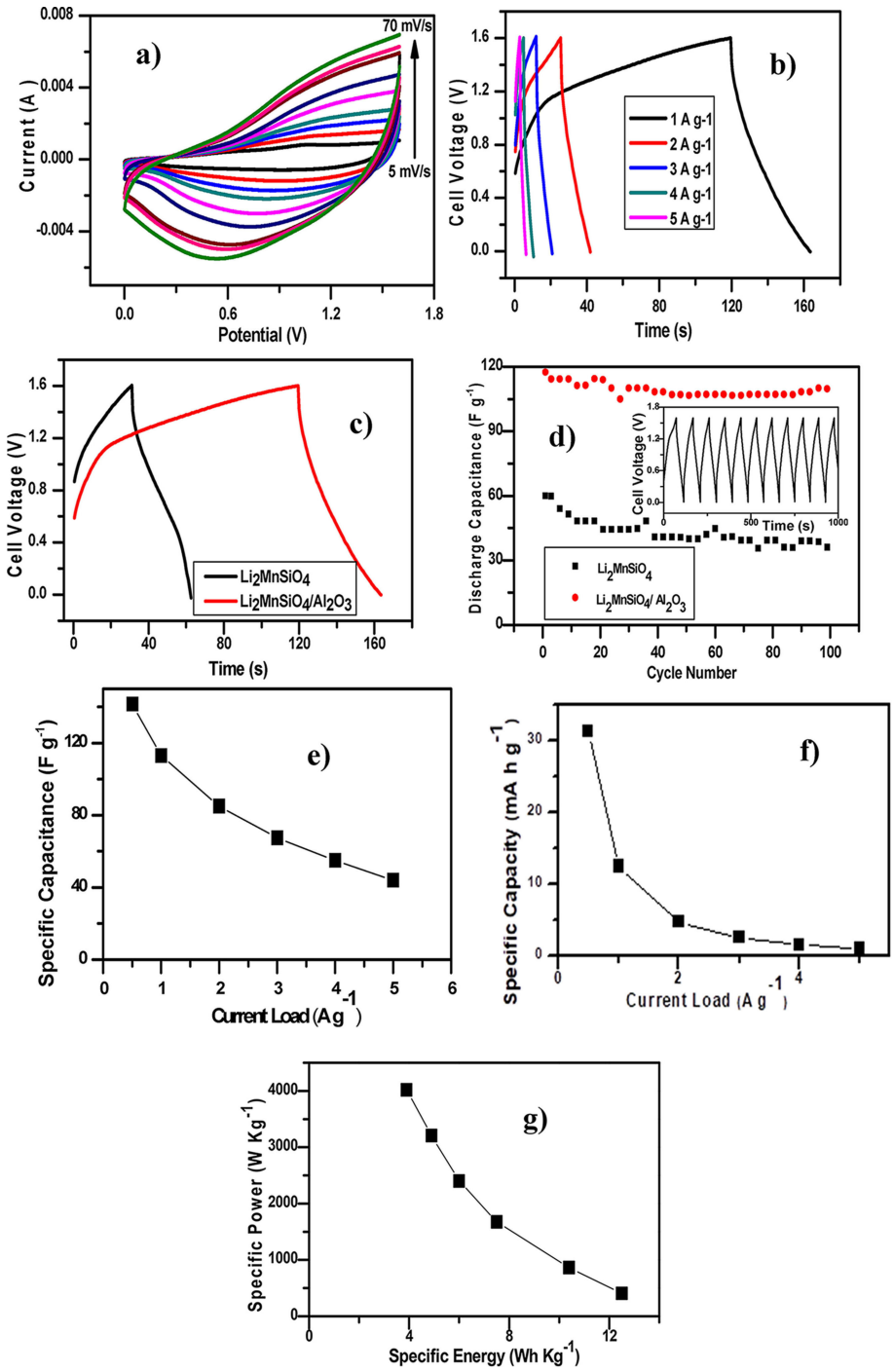


**Figure 7.** a) CV curves of the AC//$Li_2MnSiO_4/Al_2O_3$ aqueous supercapattery at different scan rates, b) Galvanostatic charge-discharge profiles of AC//$Li_2MnSiO_4/Al_2O_3$ hybrid cells at different current load values, c) Comparative plot of galvanostatic charge-discharge profiles of LMS and LMSA aqueous hybrid cells at current load of 1 A $g^{-1}$, d) Cycling performance of aqueous supercapatteries with continuous charge-discharge profiles of the nanocomposite hybrid cell as inset, Rate capability in terms of e) capacitance and f) capacity of hybrid cells at various current loads and g) the Ragone plot of aqueous supercapattery at various current loads.

10.4 W h $kg^{-1}$ and a high specific power of 864.3 W $kg^{-1}$ at a current load of 1 A $g^{-1}$. Notably, the electrochemical performance of our nanocomposite hybrid system is comparable to other reported supercapatteries and even better than some reported studies. This work demonstrates the potential of nanocomposite $Li_2MnSiO_4/Al_2O_3$ as a high rate supercapattery electrode and offers good prospects for developing energy storage devices with good cycling stability and high specific power.


© 2018 Wiley-VCH Verlag GmbH & Co. KGaA, Weinheim

25666223, 2018, 6, Downloaded from https://chemistry-europe.onlinelibrary.wiley.com/doi/10.1002/batt.201800045 by University of Ulsan, Wiley Online Library on [11/11/2025]. See the Terms and Conditions (https://onlinelibrary.wiley.com/terms-and-conditions) on Wiley Online Library for rules of use; OA articles are governed by the applicable Creative Commons License

25666223, 2018, 6, Downloaded from https://chemistry-europe.onlinelibrary.wiley.com/doi/10.1002/batt.201800045 by University of Ulsan, Wiley Online Library on [11/11/2025]. See the Terms and Conditions (https://onlinelibrary.wiley.com/terms-and-conditions) on Wiley Online Library for rules of use; OA articles are governed by the applicable Creative Commons License

## Experimental Section

### Synthesis of $Li_2MnSiO_4/Al_2O_3$

A hydrothermal synthetic route was employed for the synthesis of LMS nanoparticles using stoichiometric amounts of LiOH (Sigma Aldrich, 98 1%), $MnCl_2.4H_2O$ (Sigma Aldrich, 99.99%) and $SiO_2$ nanoparticles (Aldrich, 99.5%) in a molar ratio of 4:1:1. Typically, silicon dioxide nanoparticles were dispersed in 15 mL oxygen free deionised water for 1 h. Thereafter, solutions of LiOH and $MnCl_2.4H_2O$ were added to the $SiO_2$ dispersion with vigorous stirring. The mixture was allowed to stir for 1 h, then sealed in a 25 mL Teflon-lined autoclave under auto-generated pressure for 6 h at 200 °C. After the hydrothermal treatment was completed, the resulting particles were purified by centrifuging, rinsed severally with water and ethanol and dried overnight under vacuum at 80 °C to obtain the powder. The LMS nanoparticles were finally obtained by calcining the dry powder at 750 °C in a muffle furnace for 10 h in order to get rid of any amorphous precursors or impurities introduced during synthesis.

The LMS nanoparticles were coated with a nanofilm of $Al_2O_3$ by a wet chemical route to obtain the nanocomposite LMSA cathode material. Firstly, a stoichiometric amount of aluminum isopropoxide ($C_9H_{21}O_3$) was dispersed in absolute ethanol for 2 h, followed by the addition of LMS nanoparticles to the dispersion. $5.22\times10^{-3}$ moles of LMS (1.372 g) and $1.56\times10^{-4}$ moles of $Al_2O_3$ (0.041 g) were used. The slurry was mixed vigorously for 4 h, transferred to a rotary evaporator (rotavapor) to evaporate the solvent, and then vacuum-dried for 6 h at 70 °C to obtain a powder. The resulting powder was annealed at 550 °C in a muffle furnace for 5 h to obtained the nanostructured LMS cathode coated with an alumina nanofilm. $Al_2O_3$ nanoparticles were also obtained using the same procedure.

### Material Characterization

X-ray diffraction patterns of the materials were obtained using a D8 advance diffractometer (BRUKER-AXS) employing copper Kα radiation with a wavelength of 0.154 nm, operating at a voltage of 40 kV and current of 40 mA. The surface morphology, internal ultrastructure and elemental mapping studies were performed using ZEISS ULTRA scanning electron microscope equipped with an energy dispersive spectrometer and a Tecnai $G^2F_2O$ X-Twin MAT 200 kV field emission transmission electron microscope from FEI (Eindhoven, Netherlands). Small-angle X-ray scattering measurements of LMS and LMSA were obtained using an Anton Paar SAXSpace system for sealed tubes using copper Kα radiation with a wavelength of 0,154 nm. The equipment is furnished with a one-dimensional mythen 2 position sensitive detector and a beamstop alignment. The samples were scattered at a thickness of 315 mm and the sample chamber was evacuated to below 5 mbar to avoid further air scattering. Functional groups present in the pristine and modified cathode materials were obtained using a Perkin Elmer Spectrum 100 series Attenuated Total Reflection (ATR) Fourier Transform Infrared spectrometer. The surface chemistry of the materials and the lithium local environment were investigated using a PHI 5400 X-ray Photoelectron spectrometer employing a non-monochromatic Al $K_\alpha$ source (15 kV, 300 W) with hemispherical sector analyser, and a 500 MHz Bruker Avance III HD solid-state $^7Li$ magic angle spinning (MAS) Nuclear Magnetic Resonance spectrometer equipped with a 4 mm MAS BB/1H/19F probe, operating at a $^7Li$ Larmor frequency of 194.3 MHz.

### Electrochemical Measurements

Electrochemical measurements were performed using both three and two electrode cells. For measurements in the three-electrode cell, a computer interfaced to an Epsilon electrochemical workstation from Bio Analytical systems Lafayette, USA was employed for cyclic voltammetric measurements in 1 M $LiNO_3$ aqueous electrolyte. The glassy carbon electrode with diameter of 3 mm, Ag/AgCl and the Pt wire were used as the working, reference and counter electrodes, respectively. The working electrode was prepared by dispersing 2 mg of the active material in 400 µL of N-methyl-2-pyrrolidone solvent and drop casting 10 µL of the slurry on the active surface of the glassy carbon electrode. The slurry was dried at 50 °C for 24 h under a tungsten filament lamp to evaporate the solvent. The mass loading was 0.71 mg/cm$^2$. The Cyclic voltammograms were recorded in a potential window of −1 to 1 V at different scan rates and electrochemical impedance measurements were obtained using the CH Instruments, Inc Electrochemical work station, 600 E Potentiostat from USA at a frequency range of 0.1 Hz–100 kHz with 10 points per decade. For the two-electrode cell, the electrodes were prepared by mixing 70% of the active materials with 20% carbon black (conducting agent) and 10% polyvinylidene fluoride (binder) in few drops of anhydrous N-methyl-2-pyrrolidone. A homogenous paste was obtained using a mortar and pestle. Supercapattery cells were assembled in a Swagelok using the pristine and nanocomposite materials as the positive electrodes and activated carbon as the negative electrode in 1.0 M $LiNO_3$ electrolyte. Prior to the Swagelok assembly, the homogenous paste was coated on coin-shaped nickel foam with diameter of 20 mm using a spatula and dried at 80 °C for 12 h. The mass loading of the positive and negative electrodes were adjusted according to the charge-balance Equation (8) as shown below.

$$\frac{M^+}{M^-} = \left(\frac{C_{sp}^-}{C_{sp}^+}\right)\left(\frac{\Delta V^-}{\Delta V^+}\right) \quad (8)$$

where, $M$, $C_{sp}$ and $\Delta V$ represent the mass, the specific capacitance and the potential window obtained from the individual half-cells, respectively. The mass loading coated on nickel foam for the positive and negative electrodes was at 7.1 mg and 6.9 mg, respectively. A polypropylene film was used as the separator to avoid a short circuit. CV curves and galvanostatic charge-discharge profiles and the cycling performance of the supercapattery cells were obtained at a potential window of 1.6 V.

## Acknowledgments

*This study was funded partly by the National Nanoscience Postgraduate Teaching and Training Platform (NNPTTP) of the South African Department of Science and Technology (DST).*

## Conflict of Interest

The authors declare no conflict of interest.

**Keywords:** aqueous supercapattery · hydrothermal synthesis · $Li_2MnSiO_4$ · materials science · nanoparticles

[1] D. Du, R. Lan, K. Xie, S. Tao, *RSC Adv.* **2017**, *7*, 13304.
[2] L. Yu, G. Z. Chen, *J. Power Sources* **2016**, *326*, 604.


© 2018 Wiley-VCH Verlag GmbH & Co. KGaA, Weinheim

[3] H. Liu, L. Liao, Y. Lu, Q. Li, *Adv. Energy Mater.* **2017**, *7*, 1601248.
[4] G. Z. Chen, *Int. Mater. Rev.* **2016**, *0*, 1.
[5] H. Shao, N. Padmanathan, D. Mcnulty, *ACS Appl. Mater. Interfaces* **2016**, *3*, 4.
[6] N. Padmanathan, H. Shao, D. McNulty, C. O'Dwyer, K. M. Razeeb, *J. Mater. Chem. A* **2016**, *4*, 4820.
[7] F. Zhang, T. Zhang, X. Yang, L. Zhang, K. Leng, Y. Huang, Y. Chen, *Energy Environ. Sci.* **2013**, 1623.
[8] M. K. Singh, S. A. Hashmi, *Ionics* **2017**, 2027.
[9] H. Zou, B. Wang, F. Wen, L. Chen, *Ionics* **2017**, *23*, 1083.
[10] L. Xia, L. Yu, D. Hu, G. Z. Chen *Mater. Chem. Front.* **2017**, *1*, 584.
[11] L. Yu, G. Z. Chen, *Faraday Discuss.* **2016**, *190*, 231.
[12] S. S. Liu, L. J. Song, B. J. Yu, B. J. Wang, M. W. Li, *Electrochim. Acta* **2016**, *188*, 145.
[13] C. Hwang, T. Kim, Y. Noh, W. Cha, J. Shim, K. Kwak, K. M. Ok, K.-K. Lee, *Mater. Lett.* **2016**, *164*, 270.
[14] R. Yang, L. Wang, K. Deng, M. Lv, Y. Xu, *J. Alloys Compd.* **2016**, *676*, 260.
[15] K. Karthikeyan, V. Aravindan, S. B. Lee, I. C. Jang, H. H. Lim, G. J. Park, M. Yoshio, Y. S. Lee, *J. Power Sources* **2010**, *195*, 3761.
[16] K. Karthikeyan, V. Aravindan, S. B. Lee, I. C. Jang, H. H. Lim, G. J. Park, M. Yoshio, Y. S. Lee, *J. Alloys Compd.* **2010**, *504*, 224.
[17] Q. Cheng, W. He, X. Zhang, M. Li, *J. Mater. Chem. A* **2017**, *5*, 10772.
[18] R. J. Gummow, Y. He, *J. Power Sources* **2014**, *253*, 315.
[19] N. W. Hlongwa, C. O. Ikpo, N. Ross, M. Nzaba, M. M. Ndipingwi, P. G. L. Baker, E. I. Iwuoha, *J. Nanopart. Res.* **2016**, *44*, 90.
[20] V. Ramar, P. Balaya, *J. Power Sources* **2016**, *306*, 552.
[21] J. Zhu, Z. Tang, H. Tang, Q. Xu, X. Zhang, *J. Electroanal. Chem.* **2016**, *761*, 37.
[22] S. Liu, J. Xu, D. Li, Y. Hu, X. Liu, K. Xie, *J. Power Sources* **2013**, *232*, 258.
[23] M. Xie, R. Luo, R. Chen, F. Wu, T. Zhao, *Appl. Mater. Interfaces* **2015**, *20*, 10779.
[24] V. Aravindan, K. Karthikeyan, S. Ravi, S. Amaresh, W. S. Kim, Y. S. Lee, *J. Mater. Chem.* **2010**, *20*, 7340.
[25] K. Gao, C.-S. Dai, J. Lv, S.-D. Li, *J. Power Sources* **2012**, *211*, 97.
[26] L. Prado, M. Sriyai, M. Ghislandi, A. Barros-Timmons, K. Schulte, *J. Braz. Chem. Soc.* **2010**, *21*, 2238.
[27] W. Szczerba, R. Costo, S. Veintemillas-Verdaguer, M. del P. Morales, *J. Appl. Crystallogr.* **2017**, *50*, 481.
[28] T. Li, A. J. Senesi, B. Lee, *Chem. Rev.* **2016**, *116*, 11128.
[29] H. A. Al-Abadleh, V. H. Grassian, *Langmuir* **2003**, *19*, 341.
[30] D. Rangappa, K. D. Murukanahally, T. Tomai, A. Unemoto, I. Honma, *Nano Lett.* **2012**, *12*, 1146.
[31] J. K. Chastain, C. Roger, J. Moulder, *Handbook of X-Ray Photoelectron Spectroscopy: A Reference Book of Standard Spectra for Identification and Interpretation of XPS Data*; Physical Electronics Division, Perkin-Elmer Corporation Eden Prairie: Minnesota, **1992**
[32] Y.-X. Li, Z.-L. Gong, Y. Yang, *J. Power Sources* **2007**, *174*, 528.
[33] X. Kong, T. Mei, Z. Xing, N. Li, Z. Yuan, Y. Zhu, Y. Qian, *Int. J. Electrochem. Sci.* **2012**, *7*, 5565.
[34] G. Mali, C. Sirisopanaporn, D. Robert, *Solid State Nucl. Magn. Reson.* **2012**, *42*, 33.
[35] N. Ross, W. Hlongwa, C. Ikpo, M. Ndipingwi, P. Baker, E. I. Iwuoha, *J. Nanopart. Res.* **2016**, *44*, 10.
[36] C. Sirisopanaporn, R. Dominko, C. Masquelier, A. R. Armstrong, G. Mali, P. G. Bruce, *J. Mater. Chem.* **2011**, *21*, 17823.
[37] N. West, K. Ozoemena, C. Ikpo, P. G. L. Baker, E. I. Iwuoha, *Electrochim. Acta* **2013**, *101*, 86.
[38] M. Arroyo-deDompablo, *Chem. Mater.* **2008**, *20*, 5574–5584.
[39] H. Zhu, H. He, X. Xin, X. Ma, I. Zan, Y. Zhang, *Electrochim. Acta* **2015**, *155*, 116.
[40] J. M. Chem, S. Zhang, Z. Lin, L. Ji, Y. Li, G. Xu, L. Xue, S. Li, Y. Lu, O. Toprakci, *J. Mater. Chem.* **2012**, *22*, 14661.
[41] K. Bazzi, M. Nazri, V. M. Naik, V. K. Garg, A. C. Oliveira, P. P. Vaishnava, G. A. Nazri, R. Naik, *J. Power Sources* **2016**, *306*, 17.
[42] P. Gao, C. Zhang, G. Wen, *J. Power Sources* **2015**, *294*, 67.
[43] P. Chaturvedi, A. Sil, Y. Sharma, *Solid State Ionics* **2016**, *297*, 68.
[44] L. Guan, L. Yu, G. Z. Chen, *Electrochim. Acta* **2016**, *206*, 464.
[45] C. J. Jafta, F. Nkosi, L. Le Roux, M. K. Mathe, M. Kebede, K. Makgopa, Y. Song, D. Tong, M. Oyama, N. Manyala, S. Chen, K. I. Ozoemena, *Electrochim. Acta* **2013**, *110*, 228.

Manuscript received: June 12, 2018
Accepted manuscript online: October 1, 2018
Version of record online: October 30, 2018


© 2018 Wiley-VCH Verlag GmbH & Co. KGaA, Weinheim

25666223, 2018, 6, Downloaded from https://chemistry-europe.onlinelibrary.wiley.com/doi/10.1002/batt.201800045 by University of Ulsan, Wiley Online Library on [11/11/2025]. See the Terms and Conditions (https://onlinelibrary.wiley.com/terms-and-conditions) on Wiley Online Library for rules of use; OA articles are governed by the applicable Creative Commons License